ELSEVIER

Contents lists available at ScienceDirect

Journal of CO2 Utilization

journal homepage: www.elsevier.com/locate/jcou





Enhancing dry reforming of methane with engineered SBA-15-supported Fe-Ni alloy nanoparticles for sustainable syngas production

Qichang Meng^{a,1}, Patricia A. Loughney^{b,1}, Anuj Joshi^a, Ashin A. Sunny^a, Sonu Kumar^a, Pinak Mohapatra^a, Ashwin Kane^a, Lang Qin^a, Zhuo Cheng^a, Liang-Shih Fan^{a,*}

ARTICLE INFO

Keywords: Methane dry reforming Iron-Nickel alloy Greenhouse gas conversion Engineered SBA-15 Nanocatalyst

ABSTRACT

We present a novel approach to fabricate an iron-nickel alloy material tailored for methane dry reforming (DRM) by embedding FeNi₃ nanoparticles within an engineered SBA-15 mesoporous silica framework with a tunable structure (FeNi₃@SBA-15). This alloy material exhibits superior DRM performance, achieving impressive methane conversions exceeding 98% and 99% at temperatures of 800 °C and 900 °C respectively. Moreover, FeNi₃@SBA-15 demonstrates remarkable coking resistance and significantly outperforms the equivalent bulk catalyst. Specifically, we observe a methane conversion increase of over 400% and a carbon dioxide conversion increase of over 700% within the temperature range of 600 °C to 800 °C. Theoretical calculations reveal that coordinately unsaturated Ni atoms on FeNi₃ nanoparticles significantly promote the activation ability of C-H and C-O, leading to enhanced DRM performance. The insights gained from this study provide valuable guidance for the design of advanced alloy materials to efficiently mitigate greenhouse gases, while also opening the path towards sustainable syngas production, offering a viable and environmentally friendly approach to energy generation.

1. Introduction

The current global population and energy consumption trends suggest a rapid increase in demand for energy [1], leading to an industrial shift in the energy landscape. The use of fossil fuels to meet this demand has raised environmental concerns due to greenhouse gas emissions [2]. Carbon dioxide (CO₂) is a primary contributor to the greenhouse effect, and methane (CH₄) contributes to about 20% of global warming [3,4]. To reduce atmospheric CO2 and CH4 levels, substantial research has been conducted to identify effective methods for converting these gases into valuable products [5-7]. Syngas, a mixture of hydrogen (H2) and carbon monoxide (CO), serves as an essential intermediary for converting fossil fuels into value-added products including methanol, dimethyl ether, and liquid fuels [8-11]. Among the various technologies for syngas generation, dry reforming of methane (DRM) is a highly appealing approach for producing syngas with an H₂/CO ratio of 1.0 by converting CO2 and CH4 [12]. DRM not only utilizes the two most predominant greenhouse gases, CO2 and CH4, but also eliminates the

need for energy- and capital-intensive units such as the air separation unit (ASU). Moreover, the resulting syngas, with its lower H_2/CO ratio, is ideal for synthesizing oxygenated chemicals and hydrocarbons such as oxo-alcohols, acetic acid, and dimethyl ether [9,13,14] via Fischer-Tropsch synthesis [15].

However, the primary barrier to the commercialization of DRM is the high cost and long-term stability of the catalyst [16]. Although noble metal catalysts, including Pd, Ir, Rh, Ru, and Pt, manifest high thermal stability and activity in DRM [12,17,18], their exorbitant cost and scarcity [19] render them unsuitable for industrial use [20]. Alternatively, Ni-based catalysts are regarded as a prospective substitute for noble metals due to their affordability and high initial activity [21,22]. Alloying Ni with other metals is a desirable modification method because of the potential for further cost reduction and superior activity, selectivity, and deactivation resistance in comparison to the corresponding monometallic catalysts [23–25]. The Ni–Fe alloy has drawn particular attention for DRM owing to the cost-effectiveness of Fe, improved Ni reducibility, and long-term stability [26–28]. However, the

E-mail address: fan.1@osu.edu (L.-S. Fan).

a William G. Lowrie Department of Chemical and Biomolecular Engineering, The Ohio State University, Columbus, OH 43210, USA

b Department of Materials Science and Engineering, The Ohio State University, Columbus, OH 43210, USA

 $^{^{\}ast}$ Corresponding author.

¹ These authors have contributed equally to this work.

use of Ni-based catalysts is constrained by issues such as coke formation and sintering [29,30], limiting their adoption.

To combat these limitations, mesoporous support materials that exhibit superior thermal stability [31], high surface area, and controllable pore size and structure [32] can be employed. Encapsulating catalyst particles within the channels of mesoporous support enables particle size reduction and improved active site dispersion [33–35]. This assists in the realization of the confinement effect and improved resistance to coking [33,36,37] while also amplifying the reaction rate for highly active nanoparticles. The mesoporous structure, as a physical barrier, can also impede particle sintering and carbon deposition [33,38,39]. Among various mesoporous supports, SBA-15, a silica material with a well-ordered hexagonal pore structure, high specific surface area, and excellent thermal stability, is a favored choice for catalyst supports [40–42]. Moreover, it exhibits remarkable morphological flexibility, as its pore size and structure can be finely manipulated through alterations to the synthesis steps [32].

In this work, we report an approach to engineer an iron-nickel alloy catalyst for DRM by designing and synthesizing FeNi3 nanoparticles embedded in engineered SBA-15 (FeNi₃@SBA-15). Fig. 1 provides a schematic representation of our materials platform. The pore size and connective networks of mesopores with micropores of SBA-15 have been tuned to achieve optimal molecular diffusivity and reactivity. This tuning was achieved by controlling intermicellular interactions via surfactant choice and the synthesis temperature [32,43]. The FeNi₃@SBA-15 samples were synthesized using the wet impregnation method. We experimentally achieved over 98% and 99% CH₄ conversion at 800 °C and 900 °C, respectively. FeNi₃@SBA-15 also exhibited high coking resistance and outperformed the equivalent bulk catalyst with over 400% more CH₄ conversion and over 700% more CO₂ conversion in the temperature range of 600 °C to 800 °C. Density functional theory (DFT) computations indicate that the presence of low-coordinated Ni sites on nanostructured FeNi3 is pivotal in facilitating the cleavage of C-H and C-O bonds, leading to an enhanced decomposition of CH4 and CO2. This research could provide valuable insights into the design of high-performance catalysts for DRM for the efficient utilization of the two major greenhouse gases and potentially facilitate industrialization.

2. Experimental and computational

2.1. SBA-15 synthesis

A porosity-tunable synthesis was adapted based on previous literature [32,43] and pore-size control was achieved by altering the ratio of silicate source (tetraethyl orthosilicate, TEOS) to shape directing agent

(Pluronic acid, P123). The optimized synthesis used a TEOS: P123 ratio of 104, which was mixed with 2 M HCl (29 mL) and deionized water (15 mL). This mixture was stirred and held at 35 °C for 24 hours in the air, then transferred to a Parr vessel for a 48-hour hydrothermal hold at a reaction temperature of 80 °C. After air cooling to room temperature, the recovered paste material was separated from the excess liquid using Buchner funnel filtration. The paste was then cleaned by redispersing in ethanol, centrifugated at 6000 RPM for 5 minutes, and the excess solution was decanted. This cleaning process was repeated three times. After the final decant, the separated paste was dried for 24 hours in air at 80 °C. Finally, the solid was calcined for 8 hours in air at 550 °C. Using a mortar and pestle, the sample was ground into a fine for characterization.

2.2. FeNi3 syntheses

A solution was prepared by dissolving 6.811~g cetyl trimethyl ammonium bromide (CTAB), 0.943~g Fe(NO₃)₃•9 H₂O, and 2.037~g Ni (NO₃)₂•6 H₂O in 149.43 mL of ethanol. 0.5~g SBA-15 was introduced to the solution and stirred at 350 rpm for 24 hours. This was followed by heating the temperature to 90 °C to remove the ethanol. The intermediate precursor was subsequently heated at a ramp rate of 1 °C/min until it reached 600 °C, followed by a calcination process for 5 hours. Finally, the sample was reduced with a mixture of H₂ and Ar, with respective flow rates of 20 mL/min and 30 mL/min, at 500 °C for 5 hours. The resulting sample is marked as FeNi₃@SBA-15. For comparison, FeNi₃ was also synthesized using commercial SBA-15 (details in the supplementary information).

In a similar manner, the bulk $FeNi_3$ sample was prepared using SiO_2 power instead of SBA-15. The sample was shaped into 1 mm diameter particles and calcinated at 1000 °C for 5 hours prior to reduction. The sample is marked as $FeNi_3@SiO_2$.

2.3. Characterization methods

SBA-15 crystal structure and pore sizes were characterized with a combination of small-angle X-ray scattering (SAXS), pair distribution functions (PDF), transmission electron microscopy (TEM), and Brunauer-Emmett-Teller (BET) analysis of gas adsorption measurements. A XENOCS Xeuss 3.0 instrument (Pilatus3 300k detector) was used to gather SAXS patterns. Total X-ray scattering for PDF was collected at beamline 11-ID-B (λ = 0.2115 Å) as part of Argonne National Laboratory Advanced Photon Source (APS). A Tecnai G2–30 at 300 kV (4k CETA camera) was used to collect TEM images of unloaded SBA-15. A Micromeritics 3Flex surface analyzer was employed to perform nitrogen physisorption characterization. The sample first underwent

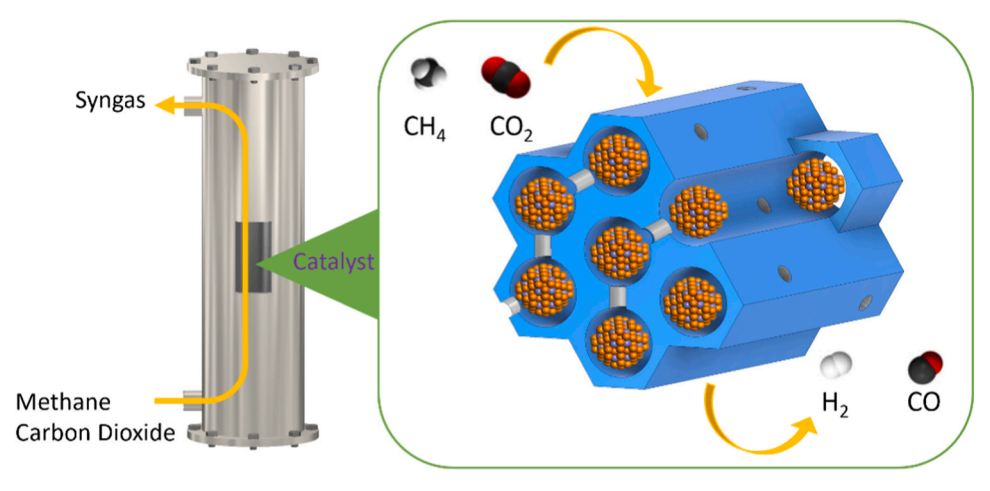


Fig. 1. Dry reforming of methane of engineered mesoporous silica SBA-15 supported FeNi₃, FeNi₃@SBA-15.

degassing on a Micromeritics SmartVacPrep device under vacuum (10^{-3} mm Hg) for 24 hours at 120°C. Then nitrogen isothermal adsorption was performed at 77 K to determine the BET surface area and t-plot micropore volume.

A combination of X-ray diffraction (XRD), PDF, TEM, and Scanning TEM-energy dispersive spectroscopy (STEM-EDS) were used for supported nanoparticle structural characterization. XRD was collected on a Rigaku SmartLab (Cu $K\alpha$) using Bragg-Brentano geometry. TEM and STEM-EDS of the supported nanocatalyst were performed on a Tecnai F20 TEM at 200 kV equipped with an Orius 2k camera. Pair distribution functions (PDFs) were collected on supported nanocatalyst samples before and after DRM measurements at the APS beamline 11-ID-B (λ = 0.2115 Å). PDF integration, reduction, and fitting were performed using a suite of software: GSAS-II [44], PDFgetx3 [45], and PDFgui [46]. PDF reduction parameters include: $Q_{max}=23.4~\text{Å}^{-1},~Q_{min}=0.1~\text{Å}^{-1},~Q_{damp}=0.037~\text{Å}^{-1},~Q_{broad}=0.030~\text{Å}^{-1},~\text{and}~r_{poly}=1.12.~Q_{damp}~\text{and}~Q_{broad}~\text{were}~\text{obtained}~\text{by}~\text{fitting}~\text{a}~\text{nickel}~\text{standard}.~\text{Fits}~\text{to}~\text{samples}~\text{were}~\text{performed}~\text{using}~\text{International}~\text{Crystal}~\text{Structure}~\text{Database}~\text{(ICSD)}~\text{structure}~\text{files}.$

2.4. Fixed bed test

DRM reactions were performed with the FeNi $_3$ @SBA-15 and FeNi $_3$ @SiO $_2$ in a U-tube reactor. For the temperature programmed reaction, 0.18 g of sample was loaded into a 0.5-inch outer diameter quartz U-shape reactor and progressively heated at a ramp rate of 5 °C/min from ambient temperature to 1000 °C. During the test, 0.5 mL/min CH4 and 0.6 mL/min CO $_2$ were introduced, and a 23.9 mL/min Ar stream was used to dilute the outlet gas. The diluted gaseous composition was analyzed using mass spectrometry. Moreover, different gas weight hourly space velocity (GHSV) was also tested with each sample at 900 °C.

2.5. Thermogravimetric analysis

Carbon deposition on FeNi₃@SBA-15 and FeNi₃@SiO₂ post DRM reaction was analyzed using a SETRAM thermogravimetric analysis (TGA) device. A sample of 11 mg, collected after 30 hours post DRM reaction at 900°C, underwent TGA with a temperature increase at a rate of 45°C/min. The oxidation phase involved exposing the sample to 50 mL/min of air and 50 mL/min of He at 800°C for one hour. In the reduction stage, a mixture of 50 mL/min H₂ and 50 mL/min He was used at 600°C for an hour. A flushing phase with 50 mL/min N₂ was applied between the oxidation and reduction stages.

2.6. Theoretical calculations

The DFT calculations were conducted using the Vienna Ab Initio Simulation Package (VASP) code [47]. The exchange-correlation potential was computed employing the Perdew-Burke-Ernzerhof functional within the generalized gradient approximation [48]. The atomic core wave functions were described using the projector-augmented wave method, with an energy cutoff of 400 eV [49]. To avoid lateral interactions, FeNi₃ nanoparticles were simulated in a three-dimensional periodic configuration using a large cubic cell with dimensions of 5×5 \times 5 nm³. Geometry optimization was performed at the Γ -point, permitting all atoms to relax until the ionic forces diminished to less than |0.01| eV Å⁻¹. The self-consistent field calculations for the electronic structure were considered converged when the difference in electronic energy between consecutive steps fell below the threshold of $1.0\,\times\,10^{-5}$ eV. To simulate the $FeNi_3$ bulk material, the $FeNi_3$ (111) surface was chosen as the model, composed of four layers of slabs segregated by a 15 Å vacuum region perpendicular to the slabs. The Climbing Image-Nudge Elastic Band (CI-NEB) method was employed with five intermediate images to locate transition states [50].

3. Results and discussion

3.1. Structural and compositional analyses of the supported nanocatalyst

To confirm the phase purity of the engineered SBA-15, its crystal and pore structures were probed (Figure S1) following its hydrothermal synthesis. TEM allows visual confirmation of ordered porosity within the SBA-15 sample with observation of pore size and wall thickness (Supplementary Figure S1a-c, Supplementary Figure S2). SAXS verifies the pore structure with three peaks at small momentum transfer values (Q) indicative of the (100), (110), and (200) reflections confirming the hexagonal pore structure (P63/mmc) for SBA-15 (Supplementary Figure S1d) [51]. Because SiO₂ SBA-15 is amorphous following the synthesis described herein and Si and O have low atomic scattering factors, total scattering is suitable to provide information on these diffuse scattering components. Total scattering collects information on both local and average structure, amorphous and crystalline materials. High-energy X-ray scattering from a synchrotron provides total scattering at a resolution possible to extract the pair distribution functions (PDF) [52]. The emergence of a few peaks in the low-r region of the PDF for the engineered SBA-15 sample reveals an amorphous structure reminiscent of bond distances in crystalline P3₂21 α-SiO₂. In particular, the PDF exhibits the most frequent Si-O bond distance at 1.6 Å (Supplementary Figure S1e), thus confirming that SBA-15 forms SiO₂ sub-

The nanoparticle growth within the engineered SBA-15 pores was performed, and characterization followed to confirm the particle growth location and the crystal structure of the alloy. The growth location for the FeNi₃ nanoparticles is confirmed to be largely within the SBA-15 pore via TEM and STEM-EDS (Fig. 2a, b). From TEM, higher contrast regions correspond to crystalline FeNi3 nanoparticles fitting within the low contrast SBA-15 pores (Fig. 2a). STEM-EDS confirms these higher contrast regions as FeNi3 surrounded by lower contrast SiO2 SBA-15 (Fig. 2b). TEM and STEM-EDS also revealed polydisperse particle sizes, where a high population of extremely small nanoparticles that fit within the 4-6 nm SBA-15 pore diameters are apparent, while a lesser population of unavoidable larger nanoparticle aggregates on the surface of some of the SBA-15 microparticles is also apparent (Fig. 2b, Supplementary Figure S3). XRD confirmed a FeNi₃ Pm3m average crystal structure for the alloy through comparison to XRD reflections for ICSD #5116 (Fig. 2c). XRD, however, gives higher crystallinity peaks than one would expect from the high degree of 4-6 nm particles fitting in SBA-15 pores from TEM. It follows that this crystallinity is coming from the larger nanoparticle aggregates, which dominate the Bragg scattering signal and ripen after DRM measurements as evidenced by the decreasing XRD peak widths. Despite the occasional presence of \sim 20 nm surface aggregates, dramatic improvements in DRM over the bulk catalyst sample are still achieved confirming the overwhelming contribution from the 4-6 nm catalysts in the SBA-15 nm pores. These results are discussed in more detail in the sections following.

In addition to the PDF collected for pure SBA-15, a PDF study was also performed on the SBA-15 embedded with FeNi $_3$ nanoparticles to gain information on both the amorphous and crystalline components. The SBA-15 Si-O nearest neighbor bond distance P3 $_2$ 21 α quartz peak is still visible at ~ 1.6 Å, while the remainder of the signal is dominated by the catalyst FeNi $_3$ alloy (Fig. 2d). The experimental PDF signal is fit to ICSD #16331 α -SiO $_2$ from 1.4 Å – 2.4 Å (Fig. 2e) while the ICSD #5116 Pm $\overline{3}$ m FeNi $_3$ is fit to the remaining signal from 2.4 Å – 60 Å using the Stepcut function [46,53]. By fitting out to r = 60Å, the slightly dampened signal for FeNi $_3$ is observable for the pre-DRM sample, corresponding to a decreased coherence length from nano-structuring. In the post-DRM sample, nanoparticle ripening is apparent during this 900°C process in the PDF signal, observable from the decreased signal dampening at high-r and increased coherence length.

Surface and pore analysis for SBA-15 and FeNi₃@SBA-15 are detailed

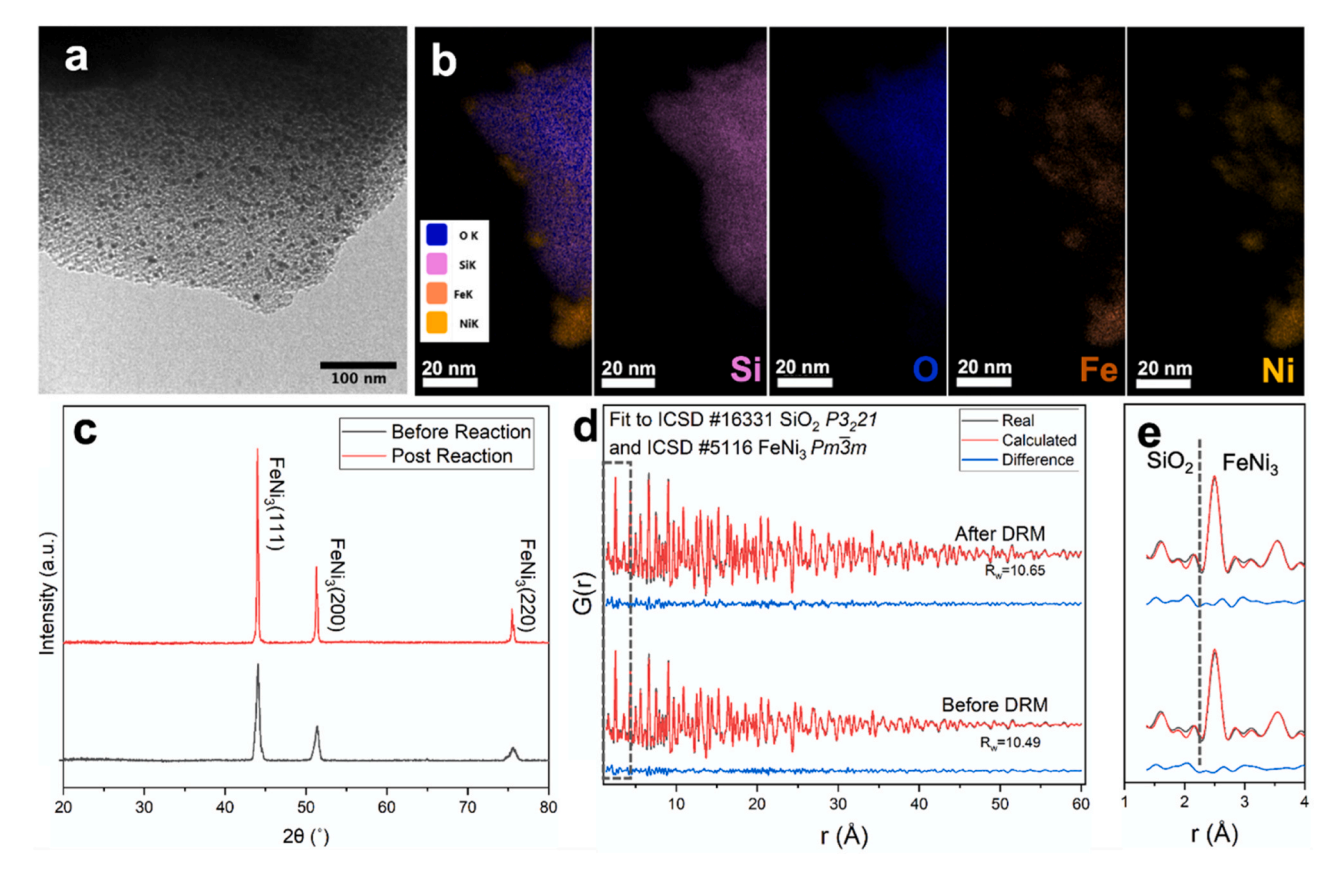


Fig. 2. FeNi₃@SBA-15 characterization including (a) TEM of SBA-15 pore channels including dispersion of small, higher contrast FeNi₃ particles within the pores, and (b) STEM-EDS confirming the SiO₂ matrix of SBA-15 containing Fe-Ni particulates. The Fe-Ni alloy is confirmed as $Pm\overline{3}m$ FeNi₃ ICSD #5116 (c) from XRD collected before and after DRM (d). Fit PDF of these samples (e) confirms the existence of both SBA-15 and FeNi₃. SBA-15 is apparent from the amorphous $P3_221$ SiO₂ signal from r = 1.4 $\mathring{A} - 2.4$ \mathring{A} while FeNi₃ is fit from r = 2.4 $\mathring{A} - 60$ \mathring{A} .

in Supplementary Table S1 and Supplementary Figure S4. The engineered SBA-15 sample gives a surface area of 630 m² g-¹, a pore volume of 0.63 cm³ g⁻¹, and a 6.1 nm uniform mesopore diameter, which is in line with TEM (Supplementary Figure S2). Additionally, it exhibits values of 180 m² g⁻¹ and 0.09 cm³ g⁻¹ for micropore area and micropore volume, respectively. The total pore volume reduced to 0.31 cm³ g⁻¹ upon loading FeNi₃ nanoparticles (FeNi₃@SBA-15), indicating their embedding inside the mesoporous SBA-15. The pore radius was at 2.65 nm with a slight decrease in magnitude, suggesting partial filling of the silica nanochannels by FeNi₃ nanoparticles. For comparison, the commercial SBA-15 is presented in Supplementary Figure S5.

3.2. Catalytic performance for methane dry reforming

The reactivity test results are presented in Fig. 3, revealing that FeNi₃@SBA-15 achieves a CH₄ conversion rate of approximately 75% at 600°C and 98% at 800°C. Conversely, FeNi₃@SiO₂ shows minimal DRM activity, with nearly zero conversion at 600°C and only an 18% CH₄ conversion rate at 800°C. Furthermore, within the temperature range of 600–800°C, the CO₂ conversion of FeNi₃@SBA-15 is over 700% higher than that of FeNi₃@SiO₂, confirming the dominant role of nanoparticles in SBA-15 in driving the reaction kinetics, despite the presence of unavoidable agglomerates as observed in Fig. 2b and S2b. At 900°C, FeNi₃@SBA-15 demonstrates higher CH₄ and CO₂ conversion rates, with

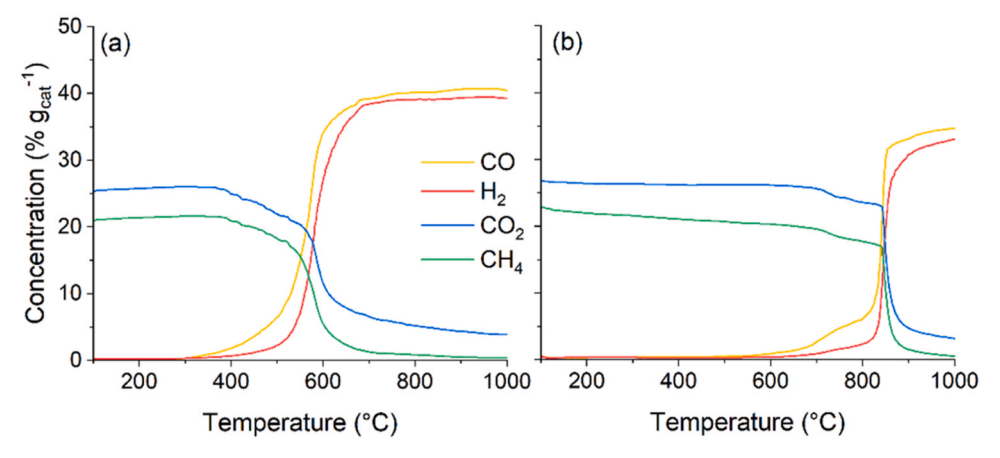


Fig. 3. Temperature programmed reaction result of FeNi₃@SBA-15(a) and FeNi₃@SiO₂(b).

the respective values of over 99% and 83%, compared with 88% and 73% for $FeNi_3@SiO_2$.

The samples were also subjected to 30-hour continuous DRM tests, and the results are shown in Fig. 4. FeNi₃@SBA-15 exhibits elevated conversion rates of CH₄ and CO₂, along with a higher H₂/CO ratio throughout the reaction due to its larger surface area, which is consistent with the BET result. The H₂/CO ratio is closer to 1, signifying the effectiveness in minimizing the side reactions. Furthermore, FeNi₃@SBA-15 demonstrates robust activity and a trend towards more stable performance at high temperature, with almost constant catalytic conversion rate observed during the test. In contrast, FeNi3@SiO2, while remaining stable phase (Supplementary Figure S6), shows gradual catalytic deactivation, with CH4 and CO2 conversion rates declining by approximately 15% after 30 hours of reaction. The observed deactivation in FeNi₃@SiO₂ may be ascribed to the accumulation of carbon deposition on the sample surface during the reaction [54], which may block the active sites of the catalyst. Conversely, FeNi₃@SBA-15 shows an absence of carbon deposition, evidenced by the complete gaseous carbon balance and unchanged weight in thermogravimetric analysis (Supplementary Figure S7). On the other hand, FeNi₃@SiO₂ demonstrates coke formation through observable weight change.

The DRM tests were also conducted under kinetic regimes with different gas hourly space velocities (GHSV), and FeNi₃@SBA-15 consistently exhibited higher reaction kinetics in all four GHSV settings (Supplementary Figure S8). At a GHSV of 2840 L g $^{-1}$ hr $^{-1}$, FeNi₃@SBA-15 exhibited approximately 52% higher conversion rates for both CH₄ and CO₂ compared to FeNi₃@SiO₂. In addition, the performance of the

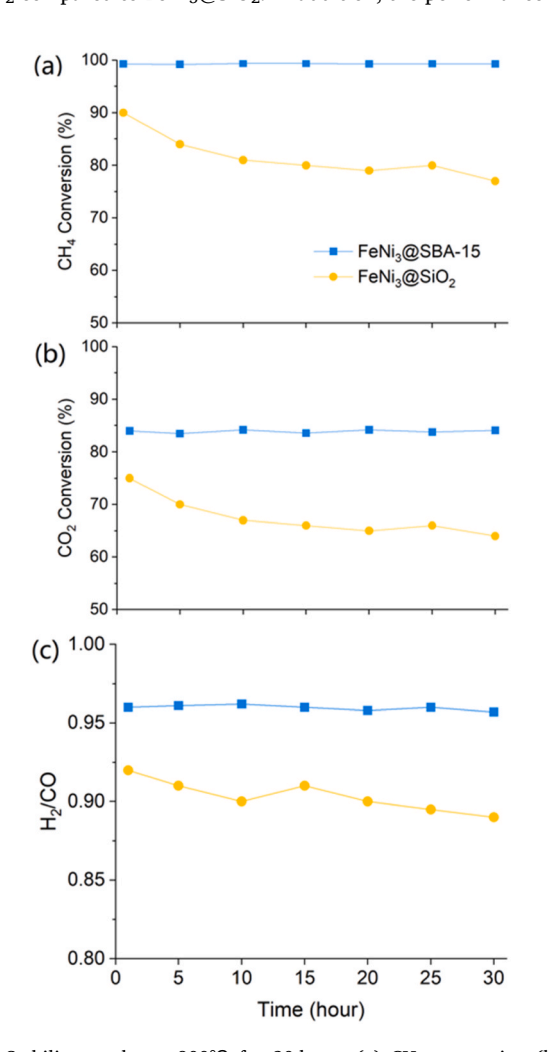


Fig. 4. Stability results at 900°C for 30 hours (a) CH_4 conversion (b) CO_2 conversion (c) H_2/CO ratio.

FeNi₃ sample loaded on commercial SBA-15 was evaluated through temperature programmed reaction (Supplementary Figure S10) in conjunction with its characterization (Supplementary Figure S9) for comparison. Our engineered SBA-15, acting as a support with a tailored structure and microporous connectivity, demonstrates enhanced reaction kinetics in DRM, surpassing that of the commercial SBA-15.

3.3. DFT reaction modeling

To gain insights into the enhanced reactivity of FeNi3 nanoparticles, we performed DFT calculations to model two systems: a (FeNi₃)₈ nanocluster (~1 nm) representing FeNi₃@SBA-15 and a FeNi₃ (111) surface representing FeNi3@SiO2. The first step in DRM involves the alloy-induced dissociation of CH4, generating hydrogen atoms (H) and CH3* radicals. These CH3* radicals then undergo further hydrogen abstraction reactions, forming CH2* and CH* intermediates. Subsequently, the CH* radicals interact with an oxygen atom (O) from CO₂, leading to the formation of CO* [55]. Fig. 5(a) illustrates the reaction network of the DRM process, encompassing three potential reaction pathways for the conversion of CH* to CO*. Path A and Path C involve the oxygenation of CH* to produce HCO* and COH*, respectively. In contrast, Path B in the DRM reaction network corresponds to the direct cleavage of the C-H bond in CH* to yield C* and H* atoms. The calculated barriers for CO* formation on the (FeNi3) nanocluster through paths A, B and C are 89.5 kJ/mol, 125.3 kJ/mol, and 116.5 kJ/mol, respectively. These results indicate that the formation of the HCO* intermediate through the binding of CH* to O* is the most favorable pathway. We further compared the complete reaction pathways through the HCO* intermediate for both the (FeNi₃)₈ nanocluster and the FeNi₃ (111) surface. The energy profile is mapped in Fig. 5(b). It is noteworthy that the energy barrier required for the initial step of CH₄ dissociation on the (FeNi₃)₈ nanoparticle is 82.7 kJ/mol, which is 24.8 kJ/mol less than what is needed on the FeNi₃ (111) surface. The (FeNi₃)₈ nanoparticle also exhibits higher activity in the dissociation of CH₃* and CH₂* radicals due to the lower barriers.

Regarding CO₂ adsorption on the FeNi₃ (111) surface, the most favorable configuration involves the binding of the C atom of CO2* to a coordinately saturated Ni atom with a relatively low adsorption energy of -32.7 kJ/mol. In contrast, for the (FeNi₃)₈ nanoparticle, the C atom of CO2* is absorbed to a coordinately unsaturated Ni atom (5-fold coordination of Ni), exhibiting a lower adsorption energy of -67.9 kJ/ mol. The energy barrier for the splitting of CO₂ into CO* and O* on the (FeNi₃)₈ nanoparticle is -32.7 kJ/mol lower compared to the FeNi₃ (111) surface. Therefore, CO₂ is more easily activated on the (FeNi₃)₈ nanoparticle. A Bader charge analysis was conducted to investigate the electron transfer behavior that affects CO2 activation. The analysis reveals that on the FeNi₃ (111) surface, a charge of 0.651|e| transfers to the adsorbed CO2 molecule from the coordinately saturated Ni site, while a charge of 0.833|e| transfers to the CO₂ from the coordinately unsaturated Ni site of the (FeNi₃)₈ nanoparticle. This suggests that the low-coordinated sites offer greater accessibility and flexibility for CO2 activation. The enhanced activation of CO2 results in a larger quantity of O* species available for the oxygenation of CH*, which explains the superior reactivity of (FeNi₃)₈ in CO formation compared to FeNi₃ (111). These findings indicate that nanostructured FeNi3 facilitates not only CH₄ dissociation but also CO₂ conversion, aligning well with experimental observations.

4. Conclusions

This work presents the synthesis of a novel catalyst material by utilizing 4–6 nm FeNi₃ nanoparticles embedded in a pore-controlled SBA-15 support. A comparative analysis of its performance in DRM reveals that the engineered FeNi₃@SBA-15 significantly outperforms the bulk FeNi₃@SiO₂ counterpart due to its larger surface area, enhanced coking resistance, and improved active sites dispersion achieved through nano-

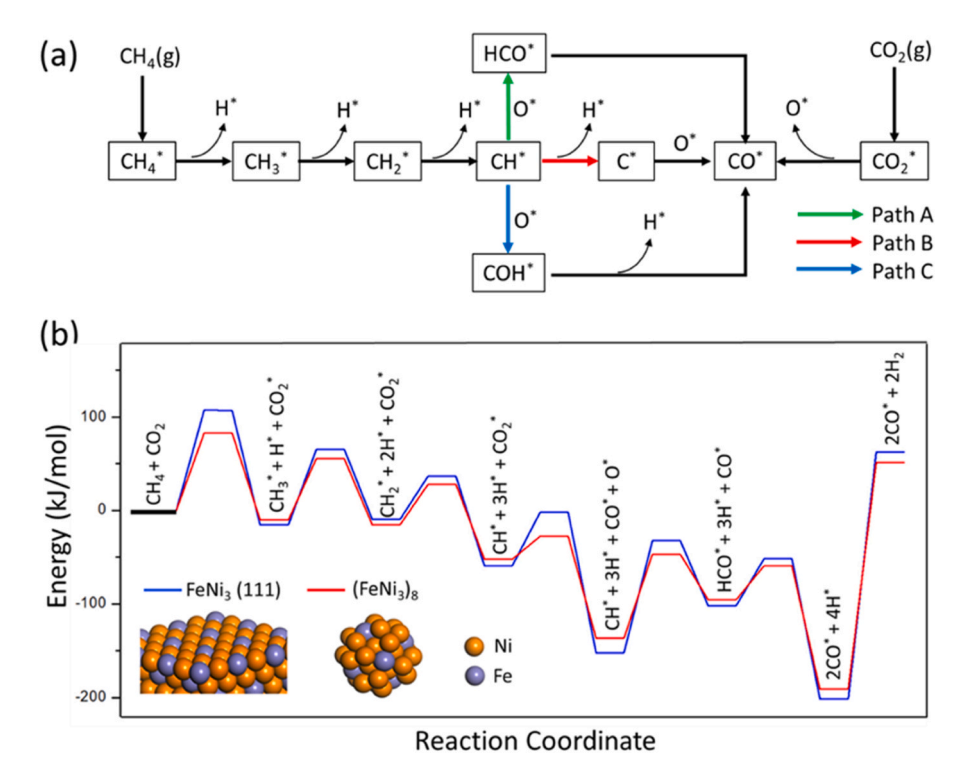


Fig. 5. (a) A schematic diagram of the reaction network of CH_4 and CO_2 to CO on $FeNi_3$ nanoparticle. (b) Calculated reaction paths for the DRM on the $(FeNi_3)_8$ nanoparticle and the $FeNi_3$ (111) surface.

structuring and tailored support. Specifically, the engineered FeNi₃@SBA-15 catalyst system achieves CH₄ conversion rates exceeding 98% and 99% at 800°C and 900°C, respectively. Moreover, in the temperature range of 600°C to 800°C, it demonstrates over 400% higher CH₄ conversion and over 700% higher CO₂ conversion compared to the equivalent bulk material. Additionally, the engineered FeNi₃@SBA-15 exhibits promising long-term catalytic activity, with higher conversion rates of CH₄ and CO₂, a favorable H₂/CO ratio, and consistent stability at high temperature, showing no signs of deactivation during the 30-hour DRM test. The DFT calculations performed in this study unveil that the FeNi₃ nanoparticle displays superior activity in the CH₄ dissociation compared to the FeNi₃ (111) surface. This enhanced activity can be attributed to lower energy barriers observed for key reaction steps. Furthermore, the Bader charge analysis indicates an increased charge transfer to CO2 on the nanoparticle, suggesting that the presence of lowcoordinated metal sites enhances the activity of CO2 splitting. These findings highlight the potential of engineered FeNi3 nanoparticles in improving DRM efficiency and promoting effective and sustainable syngas production, while also facilitating CO2 utilization.

CRediT authorship contribution statement

Zhuo Cheng: Writing – original draft, Visualization, Software. Liang-Shih Fan: Writing – review & editing, Supervision, Funding acquisition. Sonu Kumar: Writing – review & editing, Investigation. Pinak Mohapatra: Writing – review & editing. Ashwin Kane: Investigation. Lang Qin: Project administration, Conceptualization. Qichang Meng: Writing – original draft, Methodology, Investigation. Patricia A Loughney: Writing – original draft, Methodology, Investigation. Anuj Joshi: Writing – review & editing, Investigation. Ashin A Sunny: Validation, Investigation.

Declaration of Competing Interest

The authors declare the following financial interests/personal relationships which may be considered as potential competing interests:

Liang-Shih Fan reports financial support was provided by. If there are other authors, they declare that they have no known competing financial interests or personal relationships that could have appeared to influence the work reported in this paper.

Data Availability

Data will be made available on request.

Acknowledgments

The National Science Foundation (Grant No. 2029282) has supported this research. Microscopy techniques were performed at the Center for Electron Microscopy and Analysis as part of the Ohio State University. Small angle X-ray scattering data was collected at the Air Force Research Laboratory. Reported total X-ray scattering data was obtained at the Advanced Photon Source (APS) at Argonne National Laboratory beamline 11-ID-B under GUP 74463. APS beamline data was collected remotely with in-person assistance from beamline scientist Dr. Leighanne Gallington. We also thank Farshud Sorourifar and Dr. Joel Paulson for the helpful discussions.

Appendix A. Supporting information

Supplementary data associated with this article can be found in the online version at doi:10.1016/j.jcou.2024.102717.

References

- [1] S. Kılıç Depren, M.T. Kartal, N. Çoban Çelikdemir, Ö. Depren, Energy consumption and environmental degradation nexus: a systematic review and meta-analysis of fossil fuel and renewable energy consumption, Ecol. Inf. 70 (2022) 101747, https://doi.org/10.1016/J.ECOINF.2022.101747.
- [2] F. Johnsson, J. Kjärstad, J. Rootzén, The threat to climate change mitigation posed by the abundance of fossil fuels, Clim. Policy 19 (2019) 258–274, https://doi.org/ 10.1080/14693062.2018.1483885.

- [3] I.B. Ocko, V. Naik, D. Paynter, Rapid and reliable assessment of methane impacts on climate, Atmos. Chem. Phys. 18 (2018) 15555–15568, https://doi.org/ 10.5194/ACP-18-15555-2018.
- [4] I.B. Ocko, T. Sun, D. Shindell, M. Oppenheimer, A.N. Hristov, S.W. Pacala, D. L. Mauzerall, Y. Xu, S.P. Hamburg, Acting rapidly to deploy readily available methane mitigation measures by sector can immediately slow global warming, Environ. Res. Lett. 16 (2021) 054042, https://doi.org/10.1088/1748-9326/ABF9C8.
- [5] A. Joshi, V. Shah, P. Mohapatra, S. Kumar, R.K. Joshi, M. Kathe, L. Qin, A. Tong, L. S. Fan, Chemical looping-A perspective on the next-gen technology for efficient fossil fuel utilization, Adv. Appl. Energy 3 (2021), https://doi.org/10.1016/j.adapen.2021.100044.
- [6] A. Joshi, P. Mohapatra, R. Joshi, S. Kumar, A. Sunny, Z. Cheng, L. Qin, L.-S. Fan, Advances in chemical looping combustion technology, in: Combustion Chemistry and the Carbon Neutral Future, Elsevier, 2023, pp. 383–416, https://doi.org/ 10.1016/b978-0-323-99213-8.00003-5.
- [7] A.A. Sunny, Q. Meng, S. Kumar, R. Joshi, L.-S. Fan, Nanoscaled oxygen carrierdriven chemical looping for carbon neutrality: opportunities and challenges, Acc. Chem. Res 2014 (2023), https://doi.org/10.1021/ACS.ACCOUNTS.3C00517.
- [8] F. Kong, A. Tong, M.V. Kathe, L.S. Fan, D. Tomasko, Process intensification by applying chemical looping in natural gas to dimethyl ether conversion process—Implications for process design education, Chem. Eng. Process. - Process. Intensif. 143 (2019) 107566, https://doi.org/10.1016/J.CEP.2019.107566.
- [9] A.A. Al-Qadri, G.A. Nasser, H. Adamu, O. Muraza, T.A. Saleh, CO2 utilization in syngas conversion to dimethyl ether and aromatics: Roles and challenges of zeolites-based catalysts, J. Energy Chem. 79 (2023) 418–449, https://doi.org/ 10.1016/J.JECHEM.2022.12.037.
- [10] W.C. Sung, H.S. Jung, J.W. Bae, J.Y. Kim, D.H. Lee, Hydrodynamic effects on the direct conversion of syngas to methyl acetate in a two-stage fixed-bed/fluidizedbed combined reactor, J. CO2 Util. 69 (2023) 102411, https://doi.org/10.1016/J. ICOU 2023 102411
- [11] C. Park, R.K. Joshi, E. Falascino, Y. Pottimurthy, D. Xu, D. Wang, A. Sunny, S. Hwang, A.S. Joshi, P. Mohapatra, S. Kumar, Q. Zhang, Q. Meng, V. Shah, A. Tong, L.S. Fan, Biomass gasification: Sub-pilot operation of >600h with extensive tar cracking property and high purity syngas production at H2:CO ratio ~2 using moving bed redox looping technology, Fuel Process. Technol. 252 (2023) 107966, https://doi.org/10.1016/J.FUPROC.2023.107966.
- [12] A.T. Ashcroft, A.K. Cheetham, M.L.H. Green, P.D.F. Vernon, Partial oxidation of methane to synthesis gas using carbon dioxide, Nature 1991 352 6332 (352) (1991) 225–226. https://doi.org/10.1038/352225A0.
- [13] F. Kong, A. Tong, M.V. Kathe, L.S. Fan, D. Tomasko, Process intensification by applying chemical looping in natural gas to dimethyl ether conversion process—Implications for process design education, Chem. Eng. Process. - Process. Intensif. 143 (2019) 107566, https://doi.org/10.1016/J.CEP.2019.107566.
- [14] R.K. Joshi, V. Shah, L.S. Fan, Acetic acid production using calcium ferrite-assisted chemical looping gasification of petroleum coke with in situ sulfur capture, Energy Fuels 34 (2020) 16560–16571, https://doi.org/10.1021/ACS. ENERGYFUELS 0003408/ASSET/IMAGES/LARGE/FED003408 0010 JPEG
- [15] R. Zhao, X. Meng, Q. Yin, W. Gao, W. Dai, D. Jin, B. Xu, Z. Xin, Effect of precursors of fe-based fischer-tropsch catalysts supported on expanded graphite for CO2hydrogenation, ACS Sustain Chem. Eng. 9 (2021) 15545–15556, https://doi.org/10.1021/ACSSUSCHEMENG.1C05609/SUPPL FILE/SCIC05609 SI 001.PDF.
- [16] A. Abdulrasheed, A.A. Jalil, Y. Gambo, M. Ibrahim, H.U. Hambali, M.Y. Shahul Hamid, A review on catalyst development for dry reforming of methane to syngas: recent advances, Renew. Sustain. Energy Rev. 108 (2019) 175–193, https://doi.org/10.1016/J.RSER.2019.03.054.
- [17] A. Erdöhelyi, J. Cserényi, F. Solymosi, Activation of CH4 and Its reaction with CO2 over supported Rh catalysts, J. Catal. 141 (1993) 287–299, https://doi.org/ 10.1006/JCAT.1993.1136.
- [18] P. Ferreira-Aparicio, C. Márquez-Alvarez, I. Rodríguez-Ramos, Y. Schuurman, A. Guerrero-Ruiz, C. Mirodatos, A transient kinetic study of the carbon dioxide reforming of methane over supported ru catalysts, J. Catal. 184 (1999) 202–212, https://doi.org/10.1006/JCAT.1999.2439.
- [19] A. Serrano-Lotina, L. Daza, Influence of the operating parameters over dry reforming of methane to syngas, Int. J. Hydrog. Energy 39 (2014) 4089–4094, https://doi.org/10.1016/J.IJHYDENE.2013.05.135.
- [20] A.G.S. Hussien, K. Polychronopoulou, A review on the different aspects and challenges of the dry reforming of methane (DRM) reaction, Page 3400 12, Nanomaterials 2022 Vol. 12 (2022) 3400, https://doi.org/10.3390/ NANO12193400.
- [21] P. Wang, S. Wei, S. Wang, R. Lin, X. Mou, Y. Ding, Interface-directed epitaxially growing nickle ensembles as efficient catalysts in dry reforming of methane, J. Energy Chem. 66 (2022) 502–513, https://doi.org/10.1016/J. JECHEM.2021.08.065.
- [22] L. Baharudin, N. Rahmat, N.H. Othman, N. Shah, S.S.A. Syed-Hassan, Formation, control, and elimination of carbon on Ni-based catalyst during CO2 and CH4 conversion via dry reforming process: a review, J. CO2 Util. 61 (2022) 102050, https://doi.org/10.1016/J.JCOU.2022.102050.
- [23] L. Lyu, M. Shengene, Q. Ma, J. Sun, X. Gao, H. Fan, J. Zhang, T.S. Zhao, Synergy of macro-meso bimodal pore and Ni-Co alloy for enhanced stability in dry reforming of methane, Fuel 310 (2022) 122375, https://doi.org/10.1016/J. FUEL.2021.122375.
- [24] M. Cichy, M. Pańczyk, G. Słowik, W. Zawadzki, T. Borowiecki, Ni–Re alloy catalysts on Al2O3 for methane dry reforming, Int. J. Hydrog. Energy 47 (2022) 16528–16543, https://doi.org/10.1016/J.IJHYDENE.2022.03.147.

- [25] V.K. Velisoju, Q.J.S. Virpurwala, Y. Attada, X. Bai, B. Davaasuren, M. Ben Hassine, X. Yao, G. Lezcano, S.R. Kulkarni, P. Castano, Overcoming the kinetic and deactivation limitations of Ni catalyst by alloying it with Zn for the dry reforming of methane, J. CO2 Util. 75 (2023) 102573, https://doi.org/10.1016/J. JCOU.2023.102573.
- [26] B. Li, Y. Luo, B. Li, X. Yuan, X. Wang, Catalytic performance of iron-promoted nickel-based ordered mesoporous alumina FeNiAl catalysts in dry reforming of methane, Fuel Process. Technol. 193 (2019) 348–360, https://doi.org/10.1016/J. FUPROC 2019 05 033
- [27] X. Yao, Q. Cheng, Y. Attada, S. Ould-Chikh, A. Ramírez, X. Bai, H.O. Mohamed, G. Li, G. Shterk, L. Zheng, J. Gascon, Y. Han, O.M. Bakr, P. Castaño, Atypical stability of exsolved Ni-Fe alloy nanoparticles on double layered perovskite for CO2 dry reforming of methane, Appl. Catal. B 328 (2023) 122479, https://doi.org/10.1016/1.APCATR.2023.122479
- [28] X. Fang, L. Mao, L. Xu, J. Shen, J. Xu, X. Xu, X. Wang, Ni-Fe/La2O3 bimetallic catalysts for methane dry reforming: Elucidating the role of Fe for improving coke resistance, Fuel 357 (2024) 129950, https://doi.org/10.1016/J. FUEL.2023.129950.
- [29] J.M. Ginsburg, J. Piña, T. El Solh, H.I.De Lasa, Coke formation over a nickel catalyst under methane dry reforming conditions: Thermodynamic and kinetic models, Ind. Eng. Chem. Res 44 (2005) 4846–4854, https://doi.org/10.1021/ IE0496333/ASSET/IMAGES/MEDIUM/IE0496333E00040.GIF.
- [30] Z. Bian, S. Das, M.H. Wai, P. Hongmanorom, S. Kawi, A review on bimetallic nickel-based catalysts for CO2 reforming of methane, ChemPhysChem 18 (2017) 3117–3134, https://doi.org/10.1002/cphc.201700529.
- [31] D. Zhao, J. Feng, Q. Huo, N. Melosh, G.H. Fredrickson, B.F. Chmelka, G.D. Stucky, Triblock copolymer syntheses of mesoporous silica with periodic 50 to 300 angstrom pores, Science (1979) 279 (1998) 548–552, https://doi.org/10.1126/ SCIENCE.279.5350.548/ASSET/F429A4F4-DACE-4061-B204-8E1CEA6F9EC7/ ASSETS/GRAPHIC/SE0286194007.JPEG.
- [32] A. Galarneau, H. Cambon, F. Di Renzo, F. Fajula, True microporosity and surface area of mesoporous SBA-15 silicas as a function of synthesis temperature, Langmuir 17 (2001) 8328–8335, https://doi.org/10.1021/LA0105477/ASSET/IMAGES/ LARGE/LA0105477F00009.JPEG.
- [33] O. Daoura, G. Fornasieri, M. Boutros, N. El Hassan, P. Beaunier, C. Thomas, M. Selmane, A. Miche, C. Sassoye, O. Ersen, W. Baaziz, P. Massiani, A. Bleuzen, F. Launay, One-pot prepared mesoporous silica SBA-15-like monoliths with embedded Ni particles as selective and stable catalysts for methane dry reforming, Appl. Catal. B 280 (2021) 119417, https://doi.org/10.1016/J. APCATB.2020.119417.
- [34] L. Qin, L.S. Fan, Y. Liu, J. Pan, Y.Y. Chen, J.W. Goetze, D. Xu, J.A. Fan, SBA-16-mediated nanoparticles enabling accelerated kinetics in cyclic methane conversion to syngas at low temperatures, ACS Appl. Energy Mater. 3 (2020) 9833–9840, https://doi.org/10.1021/ACSAEM.0C01495/ASSET/IMAGES/LARGE/AE0C01495 M021.JPEG.
- [35] K.S. Park, T.Y. Goag, J.H. Kwon, Y.M. Park, J.S. Yu, H.E. Jeong, J.W. Choung, J. W. Bae, Effects of spatially confined nickel nanoparticles in surface-pretreated hydrophobic SBA-15 for dry reforming of CH4 with CO2, J. CO2 Util. 51 (2021) 101629, https://doi.org/10.1016/J.JCOU.2021.101629.
- [36] C.C. Chong, S.N. Bukhari, Y.W. Cheng, H.D. Setiabudi, A.A. Jalil, C. Phalakornkule, Robust Ni/Dendritic fibrous SBA-15 (Ni/DFSBA-15) for methane dry reforming: effect of Ni loadings, Appl. Catal. A Gen. 584 (2019) 117174, https://doi.org/ 10.1016/1.APCATA 2019.117174
- [37] L. Karam, N. El Hassan, Advantages of mesoporous silica based catalysts in methane reforming by CO2 from kinetic perspective, J. Environ. Chem. Eng. 6 (2018) 4289–4297, https://doi.org/10.1016/J.JECE.2018.06.031.
- [38] Q. Song, R. Ran, X. Wu, Z. Si, D. Weng, Dry reforming of methane over Ni catalysts supported on micro- and mesoporous silica, J. CO2 Util. 68 (2023) 102387, https://doi.org/10.1016/J.JCOU.2022.102387.
- [39] W. Liu, L. Li, S. Lin, Y. Luo, Z. Bao, Y. Mao, K. Li, D. Wu, H. Peng, Confined Ni-In intermetallic alloy nanocatalyst with excellent coking resistance for methane dry reforming, J. Energy Chem. 65 (2022) 34–47, https://doi.org/10.1016/J. JECHEM.2021.05.017.
- [40] S. Singh, R. Kumar, H.D. Setiabudi, S. Nanda, D.V.N. Vo, Advanced synthesis strategies of mesoporous SBA-15 supported catalysts for catalytic reforming applications: A state-of-the-art review, Appl. Catal. A Gen. 559 (2018) 57–74, https://doi.org/10.1016/J.APCATA.2018.04.015.
- [41] P.A. Loughney, V. Doan-Nguyen, Synthesis of nanostructured materials for conversion of fuels, ACS Symp. . Ser. 1364 (2020) 189–206, https://doi.org/ 10.1021/BK-2020-1364.CH007.
- [42] Y. Liu, L. Qin, Z. Cheng, J.W. Goetze, F. Kong, J.A. Fan, L.S. Fan, Near 100% CO selectivity in nanoscaled iron-based oxygen carriers for chemical looping methane partial oxidation, 1–6, Nat. Commun. 10 (1) (2019) 10, https://doi.org/10.1038/S41467-019-13560-0.
- [43] P. Van Der Voort, M. Benjelloun, E.F. Vansant, Rationalization of the synthesis of SBA-16: controlling the micro- and mesoporosity, J. Phys. Chem. B 106 (2002) 9027–9032, https://doi.org/10.1021/JP0261152/ASSET/IMAGES/LARGE/ JP0261152F00006.JPEG.
- [44] B.H. Toby, R.B. Von Dreele, GSAS-II: the genesis of a modern open-source all purpose crystallography software package, Urn:Issn:0021-8898 46 (2013) 544–549. (https://doi.org/10.1107/S0021889813003531).
- [45] P. Juhás, T. Davis, C.L. Farrow, S.J.L. Billinge, PDFgetX3: a rapid and highly automatable program for processing powder diffraction data into total scattering pair distribution functions, Urn:Issn:0021-8898 46 (2013) 560–566. (https://doi.org/10.1107/S0021889813005190).

- [46] C.L. Farrow, P. Juhás, J.W. Liu, D. Bryndin, E.S. Božin, J. Bloch, T. Proffen, S.J.L. Billinge, PDFgui user guide 2.0 release May 2023, (2006). (https://www.diffpy.org) (accessed May 28, 2023).
- [47] G. Kresse, J. Furthmiiller B', Efficiency of ab-initio total energy calculations for metals and semiconductors using a plane-wave basis set, 1996.
- [48] J.P. Perdew, K. Burke, M. Ernzerhof, Generalized Gradient Approximation Made Simple, Phys. Rev. Lett. 77 (1996) 3865, https://doi.org/10.1103/ PhysRevLett. 77 3865
- [49] G. Kresse, D. Joubert, From ultrasoft pseudopotentials to the projector augmentedwave method, Phys. Rev. B 59 (1999) 1758, https://doi.org/10.1103/ PhysRevB.59.1758.
- [50] D. Sheppard, G. Henkelman, Paths to which the nudged elastic band converges, J. Comput. Chem. 32 (2011) 1769–1771, https://doi.org/10.1002/JCC.21748.
- [51] W.J.J. Stevens, K. Lebeau, M. Mertens, G. Van Tendeloo, P. Cool, E.F. Vansant, Investigation of the morphology of the mesoporous SBA-16 and SBA-15 materials, J. Phys. Chem. B 110 (2006) 9183–9187, https://doi.org/10.1021/JP0548725/ ASSET/IMAGES/LARGE/JP0548725F00009.JPEG.
- [52] J. Rantanen, D. Majda, J. Riikonen, V.P. Lehto, The atomic local ordering of SBA-15 studied with pair distribution function analysis, and its relationship to porous structure and thermal stability, Acta Mater. 175 (2019) 341–347, https://doi.org/ 10.1016/J.ACTAMAT.2019.06.005.
- [53] C.L. Farrow, P. Juhas, J.W. Liu, D. Bryndin, E.S. Boin, J. Bloch, T. Proffen, S.J. L. Billinge, PDFfit2 and PDFgui: computer programs for studying nanostructure in crystals, J. Phys.: Condens. Matter 19 (2007) 335219, https://doi.org/10.1088/0953-8984/19/33/335219.
- [54] K. Ray, S. Sengupta, G. Deo, Reforming and cracking of CH4 over Al2O3 supported Ni, Ni-Fe and Ni-Co catalysts, Fuel Process. Technol. 156 (2017) 195–203, https://doi.org/10.1016/J.FUPROC.2016.11.003.
- [55] L. Foppa, M.C. Silaghi, K. Larmier, A. Comas-Vives, Intrinsic reactivity of Ni, Pd and Pt surfaces in dry reforming and competitive reactions: Insights from first principles calculations and microkinetic modeling simulations, J. Catal. 343 (2016) 196–207, https://doi.org/10.1016/J.JCAT.2016.02.030.